Comparison of intermolecular interactions in two phases of MeNSOF2

Citation for published version:
Mews, R & Parsons, S 2014, 'Comparison of intermolecular interactions in two phases of MeNSOF2' Zeitschrift für Kristallographie - Crystalline Materials, vol. 229, no. 9, pp. 649–660. DOI: 10.1515/zkri-2014-1733

Digital Object Identifier (DOI):
10.1515/zkri-2014-1733

Link:
Link to publication record in Edinburgh Research Explorer

Document Version:
Peer reviewed version

Published In:
Zeitschrift für Kristallographie - Crystalline Materials

Cite as:
Mews, R., & Parsons, S. (2014). Comparison of intermolecular interactions in two phases of $MeNSOF_2$. *Zeitschrift für Kristallographie - Crystalline Materials*, 229(9), 649–660.

Manuscript received: 06.02.2014; Accepted: 24.06.2014; Article published: 05.08.2014

Comparison of intermolecular interactions in two phases of $MeNSOF_2$**

Rüdiger Mews[1] and Simon Parsons[2,*]

[1]Institute of Inorganic Chemistry, Bremen University, Leobenerstrasse NW2, D-28359 Bremen, Germany.

[2]EaStCHEM, School of Chemistry, Joseph Black Building, University of Edinburgh, West Mains Road, Edinburgh, EH9 3FJ, UK.

[*]Corresponding author; tel: +44-(0)131 650 4806, fax: +44-(0)131 650 4743, e-mail: s.parsons@ed.ac.uk

[**]We thank EPSRC for funding and Dr Keith Refson (ISIS Facility) for his advice on phonon calculations in CASTEP and Professor Branton Campbell (Brigham Young University) for advice on distortion mode analysis.

Supporting information:
Electronic supporting information available from the author.

Graphical abstract:

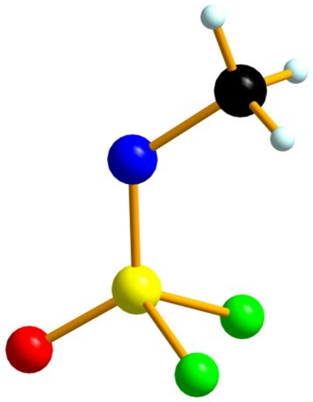

Synopsis:
$MeNSOF_2$ is an analogue of SO_2F_2 with one O= replaced by MeN=. The triclinic phase grown at 150 K transforms slowly to a denser monoclinic phase at 140 K which has stronger dispersion interactions. The triclinic phase is favoured by entropy because of its ‘looser’ structure

Abstract

$MeNSOF_2$ was crystallised by laser-assisted zone refinement at 150 K. The structure obtained by X-ray diffraction initially on cooling to 140 K was triclinic, *P*-1, but this transformed slowly to a second phase, which was monoclinic *C*2/*c*. Bond distances and angles are similar to equivalent interactions in $(MeN)_2SF_2$ and SO_2F_2. Intermolecular interactions in both phases are dominated by dispersion, though electrostatics are also important in all the most energetic contacts. Though no interatomic contacts fall within the sums of van der Waals radii of the contacting atoms, PIXEL calculations indicate that some intermolecular energies are similar to medium-strength hydrogen bonds. The monoclinic phase is denser than the triclinic phase, having stronger dispersion interactions. PIXEL and DFT calculations indicate that the two phases are energetically very finely balanced, but phase I becomes competitive at higher temperature on account of the entropy advantage of its 'looser' structure. DFT phonon energy calculations suggest that the mechanism of the transition may involve coupling between acoustic and low energy optical phonons.

1. Introduction

Though we are not aware of any systematic studies on the subject, it seems, anecdotally, that polymorphism and phase transitions are more common phenomena in simple molecular materials than they are in more complex systems. Water, with 13 different crystalline phases under varying conditions of temperature and pressure, is an extreme illustration, but the crystal structures of simple organic compounds can also display 'archetypal' behaviour, showing a variety of intermolecular motifs in different phases which are characteristic for whole families of compounds. For example, acetone[1] shows two phases under different conditions of temperature and pressure which exhibit all three of the common dipolar carbonyl-carbonyl motifs.[2]

In this paper we describe the crystallographic studies of *N*-methylimido-sulfuroxide difluoride, $MeN{=}SOF_2$. The properties of sulfuroxide difluoride imides are strongly dependent on the substituents R. With electron withdrawing groups (e,g-SF_5, FSO_2, CN) the $NSOF_2$ group acts as F^- acceptor. With strong fluoride ion donors, the tetracoordinated sulfur centres transform to pentacoordinated sulfur oxide trifluoride imides $RNSOF_3^-$.[3] $MeNSOF_2$[4] acts as a versatile N-donor: in super acids $[H_3CN(H)\ SOF_2]^+$ is formed, and with AF_5 (A = As, Sb) the adducts $F_5A\text{-}N(H_3C)SOF_2$ were isolated and structurally characterised.[5] The versatility of the $NSOF_2$ group is shown in the series $[NSOF_2]^-$,[6] H_3CNSOF_2,[4] $[(H_3C)_2NSOF_2]^+$,[7] $[H_3CN(SOF_2)\ Re(CO)_5]^+$,[8] $[Mn[(CO)_5NSOF_2)$, and $[Mn(CO)_4NSOF_2]_2$.[9] On the other hand this versatility causes problems for the precise determination of geometrical data. For $[NSOF_2]^-$ (with TAS+ as non-coordinating counterion)

N/O/F disorder is observed. Theoretical calculations suggest that $RNSOF_2$ derivatives are subject to substituent dependent equllibria between *syn*- and *anti*- conformers.

Highly efficient synthetic routes to sulfuroxide difluoride imides start with OSF_4. From the reactions with primary amines or N,N-bis-silylated amines, with $Me_3SiNCNSiMe_3$ or $Si(NCO)_4$ the derivatives FSO_2NSOF_2,[10,11] F_5SNSOF_2,[12,13] $NCNSOF_2$,[14-16] and $FC(O)NSOF_2$[17,18] were isolated. These materials have been structurally characterised by gas-phase electron diffraction, but because of their low melting points, data on their solid-state structures is more limited, and of the compounds listed, only one in case, $FC(O)NSOF_2$, was the crystal structure also reported. $MeNSOF_2$ is also a liquid at room temperature, and determination of its crystal structure therefore required use of *in situ* crystal growth methods.

We show that $MeNSOF_2$ initially crystallises in a phase which transforms slowly into a second crystalline form. In addition to describing the molecular structure of the compound itself in the solid state we will also attempt to rationalise why these two crystals structures should be thermodynamically competitive. Established methods for ‘rationalising’ crystal structures are based on analysis of intermolecular contacts, comparing them to sums of van der Waals radii. The most common of the standard sets of radii has reached an impressively high state of antiquity.[19]

More recent approaches to the problem of analysing crystal packing emphasise the importance of total molecule-molecule interactions rather than individual atom-atom contacts. These approaches may take the form of explicit energy calculations using quantum mechanical techniques[20] or the simpler but equally accurate PIXEL method, which has the great advantage of partitioning total energies into chemically meaningful components: electrostatic, dispersion etc.[21-25] Other methods include topological analysis where space in a crystal structure is partitioned into Voronoi-Dirichlet polyhedra;[26-28] in this case strong intermolecular interactions are manifested by shared polyhedral faces with large areas, but the method also enables structures to be classified and compared with archetypal motifs such as cubic and hexagonal close-packing. In Hirshfeld surface analysis[29,30] a crystal structure is also partitioned, but here the partitioning scheme is based on electron density. It enables a molecular surface to be defined, and when combined with other properties such as distance, topological measures or electrostatic potential, it provides a powerful method for visualising the factors which influence the geometry of intermolecular interactions.

The stability of molecular crystal structures is often analysed by considering hydrogen bonding. H-bonds are easy to recognise, and while they are certainly important, other interactions with less characteristic geometric features may be over-looked.[19] It is the ability of the molecule-molecule approaches mentioned above to see beyond the atom-atom view of intermolecular interactions that make them so powerful, especially in cases, such as the one described in this paper, where conventional approaches appear to suggest that there are no significant intermolecular interactions at all.

2. Experimental

2.1 Synthesis of MeNSOF$_2$

MeNSOF$_2$ was prepared by the method of Cramer and Coffman.[4] It is a colourless liquid, bp. 39°C.

2.2 Crystal growth and data collection

The sample was condensed into a thin glass capillary (o.d. 1 mm), sealed and mounted on a Bruker Apex diffractometer equipped with an Oxford Cryosystems low-temperature device. The sample was cooled to 152.5 K and freezing initiated with a swab of liquid nitrogen giving a polycrystalline solid. This was cooled to 150 K for crystal growth according to the zone melting procedure outlined by Boese using an OHCD Laser Assisted Crystal Growth Device.[31] The sample was cooled to 140 K for data collection.

Initial indexing of the diffraction pattern could be achieved with a triclinic unit cell and two orientation matrices which indexed all but 8 out of 347 reflections (CELL_NOW).[32] The relationship between the two domains was a 16° rotation about a reciprocal axis vector ~(3.5 -1.5 1), and so the sample was a split or multiple crystal rather than a twin. The data were integrated with both matrices (SAINT).[33] Integration statistics, while initially excellent for diffraction images collected in the first 1¼ h of data collection, deteriorated markedly thereafter. Indexing the later images indicated that a phase transition had occurred, giving new phase with a monoclinic *C*-centred unit cell. We shall refer to the initial triclinic phase as 'phase I', and the monoclinic phase as 'phase II'.

Out of 416 reflections harvested from the last frames in the data collection all but 29 could be indexed for phase II on one of two orientation matrices related by a 17° rotation about ~(0.03 -0.32 1.00). However, the transformation was quite slow, and the sample was mixed phase for the majority of the data collection. Data for phase II were harvested from the stronger domain only.

Following data collection at 140 K the sample was cooled to 100 K and a second data set collected. Out of 815 reflections used for indexing all but 27 could be indexed as phase II using two orientation matrices. No further phase transitions were observed. Data from the more intense domain were used for structure analysis.

2.3 Structure solution and refinement

The data-set collected on the short-lived triclinic phase I was 87% complete to 2θ = 52°. Following application of an absorption correction (TWINABS)[34] the structure was solved by Patterson methods (DIRDIF)[35] and refined by full-matrix least-squares against $|F|^2$ (CRYSTALS).[36] H-atoms were located in a difference map and refined subject to similarity restraints on the C-H distances, HCH angles and HCN angles. All non-H atoms were refined with anisotropic displacement parameters, while H-atoms were refined isotropically with U_{iso} restrained to 0.064(2) Å^2, 1.5× the equivalent isotropic displacement parameter of the carbon atom.

The structure of phase II was solved from the 100 K data set by direct methods and refined in the same way as described above, except that no restraints were applied to U_{iso}(H). The model was also refined against the phase II data-set obtained at 140 K.

Crystal and refinement data are given in Table 1.

2.4 PIXEL Calculations

Electron densities were calculated using Gaussian09[37] at the MP2 level of theory with the 6-31G** basis set using molecular geometries derived from the crystal structures with NH and CH distances changed to 1.015 and 1.089 Å, respectively. The 'normalisation' of the NH and CH distances to values typically obtained by neutron diffraction corrects approximately for the effects of asphericity of H-atom electron densities which lead to systematic shortening of distances involving hydrogen atoms when determined by X-ray diffraction. The PIXEL method, as implemented in the program OPiX,[38] was then used to calculate the intermolecular interaction energies. Atomic polarisabilities were calculated by scaling the reference values of ref [39] by a factor ($V^{\mathrm{eff}}/V^{\mathrm{free}}$) where V^{eff} is the Hirshfeld volume of an atom in the crystal structure and V^{free} is the free atom volume.[40] These factors were obtained from the DFT calculations described below. The polarisabilities obtained in this way were (in Å^3): S (2.56), N (0.97), C (1.37), O (0.74), F (0.51) and H (0.47).

2.5 Periodic DFT Calculations

DFT calculations were performed using the plane-wave pseudopotential method in the CASTEP[41] as incorporated into Material Studio package.[42] The PBE exchange-correlation functional[43] was used with norm-conserving pseudopotentials and a basis set cut-off energy of 930 eV. Brillouin zone integrations are performed with a Monkhorst-Pack[44] **k**-point grid spacing of 0.1 Å^{-1}, corresponding to a grid of 2×2×2 for phase I and 2×2×1 for phase II. These parameters gave an energy convergence of < 0.01 meV per atom for both phases. The coordinates and unit cell dimensions of both phases were optimised using the Grimme[45] and TS[46] corrections for dispersion (DFT-D)[47] starting from the experimentally determined structures. The total energy convergence tolerance was 5×10^{-6} eV/atom, with a maximum force tolerance of 0.01 eV Å^{-1}, a maximum displacement of 0.0005 Å and a maximum stress tolerance of 0.02 GPa. The space group symmetries of the two phases were retained during geometry optimisation. For subsequent frequency calculations the structure optimised with the Grimme correction was re-optimised with PBE functional, holding the cell dimensions fixed. Phonon density of state and dispersion calculations were carried out using the DFPT method[48] with Fourier interpolation.[49]

2.6 Other Programs Used

Crystal structures were visualised in MERCURY[50] and DIAMOND.[51] PLATON was used for validation and geometric analysis.[52] Hirshfeld surface analysis was carried-out using CrystalExplorer version 3.1.[53] Topological coordination sequences were determined in TOPOS,[54] and symmetry model analysis made use of the ISODISTORT web application.[55]

3. Results and discussion

3.1 General Comments

$MeNSOF_2$ has been shown to exist in two crystalline forms, a triclinic phase I and a monoclinic phase II. Both have been determined at 140 K, which facilitates comparisons between the two forms; the structure of phase II has also been determined at 100 K. At 100 K (Fig. 1) the molecules have approximate C_s symmetry, with the O2-S1-N1-C1-H11 moiety being essentially planar and the oxygen and methyl groups occupying *trans* positions across the S=N double bond. The two S-F bonds lie above and below the plane, and there is no significant difference between the S-F bond distances (Table 2). Methyl H-atoms H12 and H13 are also arranged above and below the plane. Similar comments apply to the molecular structure in both phase I and II at 140 K, and there is no statistically significant difference between any of the equivalent bond distances and angles.

Table 3 shows selected bond distances and bond angles of sulfur-oxide-fluoride-imides whose structures have been determined in the gas phase. Depending on the substituents R, the N=S distances range from 1.466(3) to 1.498(12) Å, the S=O distances from 1.385(4) to 1.424(5) Å and the SF distances from 1.529(3) to 1.549(2) Å. The S=N and S-F distances are rather similar to those in $(MeN)_2SF_2$ [S=N: 1.463(3) and 1.452(3) Å, S-F: 1.560(2), 1.570(2) Å].[56] The valence relationship of $MeNSOF_2$ with SO_2F_2 is also evident in the similarity of the S-O and S-F bond distances derived by gas phase electron diffraction [S-O: 1.397(2) Å, S-F 1.530(2) Å].[57] The largest bond angle (<N1S1O2) is formed between the two formal double bonds, as it is in SO_2F_2 [122.5(12)°]. The smallest angle (<F3S1F4) comes close to a right-angle, but is consistent with that in SO_2F_2 [96.7(11)°], being subtended by two single bonds to electronegative fluorine.

Strong electron withdrawing groups prevent anomeric interactions of the nitrogen lone pair with the SO, NS and SF bonds. This interaction strengthens the NR and the NS bond and weakens the SO and SF bonds, an effect convincingly demonstrated by comparing $MeNSOF_2$ and its AsF_5 adduct (Table 4). In the latter, the lone pair in unavailable for anomeric interactions since it is donated to AsF_5, and the SN and NC bonds become markedly longer and the SO and SF bonds shorter.

3.2 Lattice Energy Calculations

PIXEL calculations on the experimental crystal structures at 140 K give the lattice energies of phases I and II to be -61.9 and -62.1 kJ mol^{-1}, respectively, giving [$\Delta U(I \rightarrow II) = -0.2$ kJ mol^{-1}]. For both phases the balance of electrostatic (I: -19.3 vs II: -19.6 kJ mol^{-1}), polarisation (-5.5 vs -5.7), dispersion (-60.3 vs -62.5) and repulsion (23.1 vs 25.5) terms is similar, with the dispersion term the largest.

The PIXEL calculations indicate that in phase I there are nine intermolecular contacts with energies in the range -5.6 to -24.7 kJ mol^{-1}, the energy of the next strongest contact beyond this set is -2.2 kJ mol^{-1}. In phase II there are ten contacts in the range -3.8 to -26.2 kJ mol^{-1}, with the next strongest being worth -2.7 kJ mol^{-1}.

3.3 Relationship between phase I and II

The relationship between the unit cell axes in phases I and II, derived from the orientation matrices at 140 K ($\mathbf{A}_I$ and $\mathbf{A}_{II}$), can be expressed by the transformation

$$\mathbf{A}_{II}^{-1}\mathbf{A}_I \begin{pmatrix} \mathbf{a}_I \\ \mathbf{b}_I \\ \mathbf{c}_I \end{pmatrix} = \begin{pmatrix} 0.00 & 1.03 & 1.08 \\ 0.00 & 1.02 & -0.86 \\ -1.97 & 0.03 & 0.07 \end{pmatrix} \begin{pmatrix} \mathbf{a}_I \\ \mathbf{b}_I \\ \mathbf{c}_I \end{pmatrix} = \begin{pmatrix} \mathbf{a}_{II} \\ \mathbf{b}_{II} \\ \mathbf{c}_{II} \end{pmatrix}. \qquad [1]$$

The matrix shows that the relationship between the two phases can be understood in terms of a reduced or primitive setting of phase II shown in Table 5. In transforming from phase I to II the *a* axis of phase I doubles in length, while *b* and *c* equalise, leading to an overall loss of translational symmetry, but an increase in point symmetry from -1 to 2/*m*. Distortion mode analysis, in which phase II defines the high-symmetry phase and phase I with a doubled *a* axis is the low symmetry phase, shows that two modes are active, one (Γ_2^+) corresponding to rotations of molecules about the long molecular axis (see below) and the other (Γ_1^+) leading to the loss of symmetry from *C*2/*c* to *P*-1. Note that the use of the supercell for phase I is the reason that both are zone-centre (Γ) modes in this description.

3.4 Intermolecular Interactions

The relationship in Equ. 1 establishes equivalent viewing directions in the two structures. Fig. 2 shows the structure of phase I viewed along **a** with the [011] direction vertical, and phase II viewed along **c** with **a** vertical. Both structures consist of layers of molecules in which the long axes of the molecules are approximately perpendicular to the layers.

Consideration of the distribution of molecular centroids shows that the underlying topology of the layer stacking in phase I is ccp, with a molecular coordination number of 12 and a coordination sequence of 12-42-92, while that of phase II is bcc with a coordination number of 14 (coordination sequence 14-50-110). Within the layers each molecule is surrounded by six others (Fig. 3), and all of these number amongst the principal contacts in both structures. Above and below the layers, however, the departure from ideal sphere packing is more marked, and PIXEL calculations show that of the six contacts above and below the layers of phase I only three have significant energies (Fig 4 and Table 6), whereas four out of eight contacts are significant in phase II.

In phase I the layers (Fig. 3*a*) are formed by rows of molecules generated by lattice translations along **a** interacting with equivalent rows related to the first by inversion centres. The strongest interaction (to the molecule labelled 'A' in Fig. 3*a*) consists of a pair of molecules with approximately parallel but opposed dipoles. Dispersion is the largest contributing energy term (-19.1 kJ mol^{-1}) in this contact, but the electrostatic term in also significant (-13.1 kJ mol^{-1}). Other contacts are listed in Table 6. The charge-complementarity of the arrangement is demonstrated in Fig. 3c in which Hirshfeld surfaces of each molecule are shown mapped with electrostatic potential. The electrostatic potentials of the central molecule in Fig. 3*c* and three of the other five contacting molecules in the layer are also complementary, with only the weakest contacts (to molecules labelled G and H) having essentially no electrostatic stabilisation.

The layers of phase II also contain molecules surrounded by six neighbours (Fig 3b and Table 6). While the orientations of the molecules relative to the unit cell axes are different in the two phases (see Section 3.3, above), there is a strong resemblance in the strongest contacts (Fig. 3a and b). The molecules forming this contact are closer together in phase II, e.g. S1…N1 in phase I is 3.517(4) Å, but 3.443(2) in phase II, while the centroid-centroid distance is 0.05 Å shorter. The generally closer packing propagates throughout the layer, the average centroid-centroid distance being 0.21 Å shorter in phase II than in phase I. As in phase I, the electrostatic potentials are complementary (Fig. 3d) for four out of the six contacts, though the overall electrostatic energy of the six contacts is similar in both phases. However, the shorter distances result in the dispersion energy of phase II being *ca* 7 kJ mol^{-1} more negative than in phase I.

Between the layers of phase I the molecules interact in end-to-end fashion across inversion centres (Fig. 4a). The strongest interlayer contact (to molecule B, -17.1 kJ mol^{-1}) is a mixed electrostatic-dispersion interaction in which two CH_3-N moieties approach one another with opposed dipoles [H11…N1 = 2.88(3) Å]. Two dispersion interactions (to molecules F and I, -10.6 and -5.6 kJ mol^{-1}) are formed to the layer below; in the stronger contact two SOF_2 groups face each other with oppositely aligned S-O bonds [S…O = 3.537(4) Å]. The strongest interlayer contact in phase II (Fig. 4b; molecule E, -10.6 kJ mol^{-1}) is similar with S…O = 3.629(2) Å. In the contacts to molecules F and G (generated by C-centring operations, -8.6 kJ mol^{-1}) methyl groups point towards the oxygen atoms of SOF_2 groups with H12…O1 = 2.89(3) Å. In all cases electrostatic potentials in contacting molecules are complementary (Fig. 4 c and d).

Hirshfeld surface plots mapped with electrostatic potential demonstrate the role of complementary electrostatic interactions in the crystal packing of both phases: though the dominant intermolecular energy term in both phases is dispersion, the relative orientations of the molecules are determined by electrostatics. The role of electrostatic interactions in dispersion-dominated crystal structures has also been demonstrated by Spackman and co-workers,[30] while similar conclusions were drawn by Hunter and Sanders in their analysis of π stacking interactions.[58]

A second overall feature of the packing in the crystal structures described here is that in no case does any interatomic distance fall within the sums of the van der Waals radii of the contacting atoms. For example the strongest contact in phase I (to molecule A) has an energy (-24.7 kJ mol^{-1}) quite similar to a medium-strength hydrogen bond such as the OH…O interaction in phenol, but the most significant interatomic interaction distance, S1…N1 = 3.517(4) Å, is 0.17 Å longer than the sum of the van der Waals radii of S and N (3.35 Å). Unlike hydrogen bonds, dispersion interactions are often difficult to identify because they lack characteristic geometric features, and insight can really only be gained in the light of the methods summarised in the *Introduction*.

3.5 DFT Calculations

The transition from phase I to II on cooling to 140 K implies that phase II is the more enthalpically stable phase, and the small, negative difference in lattice energies calculated by PIXEL is consistent with this. However, the magnitude of the change (0.2 kJmol^{-1}), though plausible, is so small that a change in the parameters of the calculation could easily invert the energy ordering. DFT calculations were therefore carried-out with the aim of calculating the energy difference by another method, and, through calculation of the phonon frequencies, of providing some measure of the effects of entropy and zero point energy.

DFT-D geometry optimisations in which both the unit cell dimensions and the atomic coordinates were allowed to vary were carried-out using the PBE functional with both the Grimme and TS dispersion correction schemes. The optimised unit cell dimensions are given in Table 7, and compared with experimental values. The TS scheme reproduces the unit cell lengths of phase I at 140 K to within 1%, and those of phase II to within 2%, the calculated values generally being a little longer than the experimental ones. The optimised cell dimensions obtained by the Grimme scheme are up to 2.8% shorter than those obtained experimentally. The TS optimised volumes are about 1% and 3% larger than the experimental values of phases I and II, while the values obtained with Grimme's correction are about 1 and 4% smaller. Since the optimisations ignore thermal effects and effectively correspond to 0 K structures, the values obtained by the Grimme method appear more reasonable.

Both methods perform similarly in reproducing the molecular structure of $MeNSOF_2$ (Table 2). The bond distances are a little longer than those obtained experimentally, though librational shortening may account for some of the difference. Crystal Packing Similarity indices[50] for phase I at 140 K are 0.116 (Grimme) and 0.056 (TS); corresponding data for phase II at 140 K are 0.123 (Grimme) and 0.116 (TS), and 0.101 (Grimme) and 0.130 (TS) at 100 K. These data correspond to root mean square deviations of non-H atomic positions in a cluster of 15 molecules, and they demonstrate that both sets of calculations reproduce the crystal packing in both phases.

The Grimme scheme gives the correct stability ordering, with $\Delta H[I \rightarrow II]$ transition to be -8.7 kJ mol^{-1}. The TS scheme reverses the ordering, giving $\Delta H = +7.9$ kJ mol^{-1}. The air-sensitivity of $MeNSOF_2$ means that it is difficult to obtain an experimental measurement of the transition enthalpy (for example by differential scanning calorimetry), but both the PIXEL results and experience suggests that the magnitudes of both DFT estimates are rather high. Nevertheless, the more plausible unit cell dimensions and the correct energy ordering obtained with the Grimme scheme led us to use these results in subsequent calculations.

Dispersion corrections are not yet implemented in the CASTEP linear response lattice dynamics routines, and for these calculations the structure optimised with the Grimme correction was re-optimised with the uncorrected PBE functional, holding the cell dimensions fixed. The molecular geometry and crystal packing indices were essentially identical to those described above, but the energy difference was now -11.0 kJ mol^{-1}. Γ-point vibrational frequency calculations based on these re-optimised structures of phases I and II yielded positive values for all optical vibrations, with acoustic frequencies between 0 and -0.05 cm^{-1}, indicative of well-converged structures.

Integration of the phonon density of states enabled the thermal contribution to enthalpy (H), the entropy (S) and the zero-point energy (ZPE) to be evaluated (all within the harmonic approximation). The thermal contribution to free energy, $\Delta G_{\mathrm{Thermal}} = (H_2 - TS_2 + ZPE_2) - (H_1 - TS_1 + ZPE_1)$, is plotted in Fig. 5 from 0 to 155 K. The values fall between +0.18 and +0.41 kJ mol^{-1}, with entropy becoming the dominant contributor as temperature increases, $-T\Delta S$ rising from ~0 to 0.38 kJ mol^{-1}. The entropy of phase I is higher than that of phase II because it is a 'looser' structure with slightly lower vibrational frequencies. The values of $\Delta G_{\text{Thermal}}$ in Fig. 5 are not enough to overcome any of the DFT estimates of the enthalpy difference between the two phases at 0 K (-8.7 kJ mol^{-1}). However if we interpret the data in Fig. 5 in the context of the known phase transition, and set $\Delta H[I \rightarrow II] + \Delta G_{\text{Thermal}} = 0$ at the phase transition temperature (140 K), we obtain an estimate for $\Delta H[I \rightarrow II]$ of -0.35 kJ mol^{-1}, in reasonably good agreement with the value obtained from the PIXEL calculations.

Symmetry analysis indicated that two modes were active in the transition from phase I to II, leading to doubling of the crystallographic *a*-axis and molecular rotations. Though no soft modes were detected in sets of phonon dispersion curves calculated for either phase, it was notable that along the line Γ to B(½ 0 0) in phase I the frequency of the acoustic mode corresponding to vibration along the *x* direction rises to become almost degenerate with the lowest optical phonon, which, like the other optical phonons, shows almost no dispersion (Fig. 6). Since this lowest optical mode corresponds to molecular oscillations approximately parallel to the long axis of the molecule, these results suggest that the transition may be driven by acoustic-optical mode coupling.

4. Conclusions

$MeNSOF_2$, a valence analogue of SO_2F_2, is a liquid under ambient conditions. It was crystallised by *in situ* methods at 150 K. Cooling the triclinic phase I obtained at 150 K to 140 K caused a slow phase transition to occur to a monoclinic structure (phase II), characterised by doubling of the *a* axis and the reorientation of the molecules around their long axes. Intermolecular interactions in both phases are dominated by dispersion, but PIXEL calculations show that some of these interactions have energies similar to medium-strength hydrogen bonds, even though there are no interatomic distances which fall within the sums of van der Waals radii.

The PIXEL results also show that the low temperature phase (II) is only slightly (0.2 kJ mol^{-1}) more enthalpically more stable than phase I. Increased dispersion interactions which result from its higher density form an important part of this stabilisation. The lower density of phase I means that it has lower vibrational frequencies, and therefore a higher entropy. This effect dominates as temperature increases, stabilising phase I. This effect has been referred to by Gavezzotti as 'enthalpy-entropy compensation'.[25]

Direct determination of the enthalpy change of the transition by DFT depends strongly on the dispersion correction used. Indeed, the energy differences reported in this paper are all small enough that they are sensitive to changes in the computational details. Nevertheless, calculation of the thermal contributions to free energy on the basis of the phonon frequencies suggests that the energy difference at absolute zero more akin to the value obtained from the PIXEL calculations, and over an order of magnitude smaller than implied by comparison of total energies.

5. Acknowledgements

We thank EPSRC for funding and Dr Keith Refson (ISIS Facility) for his advice on phonon calculations in CASTEP and Professor Branton Campbell (Brigham Young University) for advice on distortion mode analysis.

6. References

(1) Allan, D. R.; Clark, S. J.; Ibberson, R. M.; Parsons, S.; Pulham, C. R.; Sawyer, L.: The influence of pressure and temperature on the crystal structure of acetone. *Chem. Comm.* **1999**, 751-752.

(2) Allen, F. H.; Baalham, C. A.; Lommerse, J. P. M.; Raithby, P. R.: Carbonyl-Carbonyl Interactions can be Competitive with Hydrogen Bonds. *Acta Cryst.* **1998**, *B54*, 320-329.

(3) Heilemann, W.; Mews, R.: Fluorinated sulfuramide anions. II: derivatives with penta- and psi-penta-coordinated sulfur centers. *European Journal of Solid State and Inorganic Chemistry* **1992**, *29*, 799-808.

(4) Cramer, R.; Coffman, D. D.: Iminosulfur oxydittuorides. *Journal of Organic Chemistry* **1961**, *26*, 4010-4014.

(5) Bellard, S.; Rivera, A. V.; Sheldrick, G. M.: N-Methyl-S,S-difluorosulfoximine-arsenic pentafluoride. *Acta Cryst.* **1978**, *B34*, 1034-1035.

(6) Lork, E.: Dissertation: "Untersuchungen an multifunktionellen Fluoroanionen und an SN-Mehrfachbindungssystemen. (Investigations on multifunctional fluoro anions and SN-multiple bond systms). University of Bremen, Germany, 1994.

(7) Mews, R.; Henle, H.: Amino-sulfur-fluorine derivatives as fluoride ion donors: preparation of three- and four-coordinated cations of sulfur(IV) and -(VI). *Journal of Fluorine Chemistry* **1979**, *14*, 495-510.

(8) Braeuer, H. C.: Über die Basizität Tetrakoordinierter Stickstoff-Schwefel(VI) Fluor Verbindungen (On the basicity of tetracoodinated N-S(VI)-F compounds). University of Göttingen, Germany, 1977.

(9) Buss, B.; Altena, D.; Mews, R.; Glemser, O.: Molecular structure of $[Mn(CO)_4NSOF_2]_2$, a binuclear transition metal complex with difluorooxosulfurimidato bridging ligands. *Angew. Chem. Int. Ed.* **1978**, *90*, 280-281.

(10) Glemser, O.; Roesky, H. W.; Heinze, P. R.: Synthesis of sulfur difluoride (difluorophosphinyl)-imide and sulfur oxide difluoride (fluorosulfonyl)imide. *Angew. Chem., Int. Ed.* **1967**, *6*, 710-711.

(11) Haist, R.; Alvarez, R. S. M.; Cutin, E. H.; Della Vedova, C. O.; Oberhammer, H.: Gas phase structures of N-(fluorosulfonyl)imidosulfurous difluoride, $FSO_2N{=}SF_2$, and N-(fluorosulfonyl)imidosulfuryl fluoride, $FSO_2N{=}S(O)F_2$. *Journal of Molecular Structure* **1999**, *484*, 249-257.

(12) Alvarez, R. M. S.; Cutin, E. H.; Mews, R.; Oberhammer, H.: Structure and Conformational Properties of N-Pentafluorosulfur (sulfur oxide difluoride imide) $SF_5N{=}S(O)F_2$: Vibrational Analysis, Gas Electron Diffraction, and Quantum Chemical Calculations. *J. Phys. Chem. A* **2007**, *111*, 2243-2247.

(13) Höfer, R.; Glemser, O.: New derivatives of sulfur hexafluoride. Pentafluorosulfur sulfur oxide difluoride imide $F_5S\text{-}NS(O)F_2$ and pentafluorosulfur dimethylamide $F_5S\text{-}N(CH_3)_2$. *Z. Naturforsch.* **1975**, *B30*, 458-459.

(14) Cutin, E. H.; Della Vedova, C. O.; Mack, H. G.; Oberhammer, H.: Conformation and gas-phase structure of difluorosulfenylimine cyanide, $F_2S(O)NCN$. *Journal of Molecular Structure* **1995**, *354*, 165-168.

(15) Lustig, M.; Ruff, J. K.: N-Cyanoiminosulfur oxydifluoride and N-trifluoromethyliminosulfur oxydifluoride. *Inorganic and Nuclear Chemistry Letters* **1967**, *3*, 531-533.

(16) Glemser, O.; Biermann, U.; Hoff, A.: Preparation of N-cyaniminosulfoxy difluoride. *Z. Naturforsch.* **1967**, *B22*, 893.

(17) Ruff, J. K.: N-Haliminosulfur derivatives. *Inorganic Chemistry* **1966**, *5*, 1787-1791.

(18) Boese, R.; Cutin, E. H.; Mews, R.; Robles, N. L.; Della Vedova, C. O.: ((Fluoroformyl)imido)sulfuryl Difluoride, $FC(O)N{:}S(O)F_2$: Structural, Conformational, and Configurational Properties in the Gaseous and Condensed Phases. *Inorganic Chemistry* **2005**, *44*, 9660-9666.

(19) Gavezzotti, A.: The "sceptical chymist": intermolecular doubts and paradoxes. *CrystEngComm* **2013**, *15*, 4027-4035.

(20) Stone, A.: *The Theory of Intermolecular Forces* OUP: Oxford, 2013.

(21) Dunitz, J. D.; Gavezzotti, A.: Molecular recognition in organic crystals: Directed intermolecular bonds or nonlocalized bonding? *Angew. Chem. Int. Ed.* **2005**, *44*, 1766-1787.

(22) Gavezzotti, A.: Calculation of intermolecular interaction energies by direct numerical integration over electron densities. I. Electrostatic and polarization energies in molecular crystals. *J. Phys. Chem. B* **2002**, *106*, 4145-4154.

(23) Gavezzotti, A.: Calculation of intermolecular interaction energies by direct numerical integration over electron densities. 2. An improved polarization model and the evaluation of dispersion and repulsion energies. *J. Phys. Chem. B* **2003**, *107*, 2344-2353.

(24) Gavezzotti, A.: Calculation of lattice energies of organic crystals: the PIXEL integration method in comparison with more traditional methods. *Z. Kristall.* **2005**, *220*, 499-510.

(25) Gavezzotti, A.: *Molecular Aggregation - Structure Analysis and Molecular Simulation of Crystals and Liquids*; 1st ed.; Oxford University Press: New York, 2007.

(26) Blatova, O. A.; Blatov, V. A.; Serezhkin, V. N.: A new set of molecular descriptors. *Acta Cryst.* **2002**, *B58*, 219-226.

(27) Peresypkina, E. V.; Blatov, V. A.: Topology of molecular packings in organic crystals. *Acta Cryst.* **2000**, *B56*, 1035-1045.

(28) Peresypkina, E. V.; Blatov, V. A.: Molecular coordination numbers in crystal structures of organic compounds. *Acta Cryst.* **2000**, *B56*, 501-511.

(29) McKinnon, J. J.; Spackman, M. A.; Mitchell, A. S.: Novel tools for visualizing and exploring intermolecular interactions in molecular crystals. *Acta Cryst.* **2004**, *B60*, 627-668.

(30) Spackman, M. A.; McKinnon, J. J.; Jayatilaka, D.: Electrostatic potentials mapped on Hirshfeld surfaces provide direct insight into intermolecular interactions in crystals. *CrystEngComm* **2008**, *10*, 377-388.

(31) Boese, R.; Nussbaumer, M.: *In Situ Crystallisation Techniques*; Oxford University Press, 1994.

(32) Sheldrick, G. M.: CELL_NOW. 2008-1 ed.; University of Göttingen: Göttingen, Germany, 2008.

(33) SAINT. 7 ed.; Bruker-AXS: Madison, WI, 2006.

(34) Sheldrick, G. M.: TWINABS. 2008-1 ed.; University of Göttingen: Göttingen, Germany, 2012.

(35) Beurskens, P. T.; Admiraal, G.; Beurskens, G.; Bosman, W. P.; Garcia-Granda, S.; Gould, R. O.; Smits, J. M. M.; Smykalla, C.: DIRDIF: A Computer Program System for Crystal Structure Determination by Patterson Methods and Direct Methods Applied to Difference Structure Factors.: Crystallography Laboratory, University of Nijmegen, Toernooiveld, 6525 ED Nijmegen, The Netherlands, 1992.

(36) Betteridge, P. W.; Carruthers, J. R.; Cooper, R. I.; Prout, K.; Watkin, D. J.: CRYSTALS version 12: software for guided crystal structure analysis. *J. Appl. Cryst.* **2003**, *36*, 1487.

(37) M. J. Frisch, G. W. T., H. B. Schlegel, G. E. Scuseria, M. A. Robb, J. R. Cheeseman, G. Scalmani, V. Barone, B. Mennucci, G. A. Petersson, H. Nakatsuji, M. Caricato, X. Li, H. P. Hratchian, A. F. Izmaylov, J. Bloino, G. Zheng, J. L. Sonnenberg, M. Hada, M. Ehara, K. Toyota, R. Fukuda, J. Hasegawa, M. Ishida, T. Nakajima, Y. Honda, O. Kitao, H. Nakai, T. Vreven, J. A. Montgomery, Jr., J. E. Peralta, F. Ogliaro, M. Bearpark, J. J.

Heyd, E. Brothers, K. N. Kudin, V. N. Staroverov, R. Kobayashi, J. Normand, K. Raghavachari, A. Rendell, J. C. Burant, S. S. Iyengar, J. Tomasi, M. Cossi, N. Rega, J. M. Millam, M. Klene, J. E. Knox, J. B. Cross, V. Bakken, C. Adamo, J. Jaramillo, R. Gomperts, R. E. Stratmann, O. Yazyev, A. J. Austin, R. Cammi, C. Pomelli, J. W. Ochterski, R. L. Martin, K. Morokuma, V. G. Zakrzewski, G. A. Voth, P. Salvador, J. J. Dannenberg, S. Dapprich, A. D. Daniels, Ö. Farkas, J. B. Foresman, J. V. Ortiz, J. Cioslowski, and D. J. Fox: Gaussian 09. Gaussian Inc.: Wallingford, USA, 2009.

(38) Gavezzotti, A.: OPiX. Milan, Italy, 2003; pp A computer program package for the calculation of intermolecular interactions and crystal energies, Milan, Italy, 2009.

(39) Chu, X.; Dalgarno1, A.: Linear response time-dependent density functional theory for van der Waals coefficients. *J. Chem. Phys.* **2004**, *121*, 4083-4088.

(40) Hod, O.: Graphite and Hexagonal Boron-Nitride have the Same Interlayer Distance. Why? *J. Chem. Theory Computation* **2012**, *8*, 1360-1369.

(41) Clark, S. J.; Segall, M. D.; Pickard, C. J.; Hasnip, P. J.; Probert, M. J.; Refson, K.; Payne, M. C.: First principles methods using CASTEP. *Z. Kristall.* **2005**, *220*, 567-570.

(42) Inc, A.: Materials Studio version 7. Accelrys Software Inc.: Materials Studio, Cambridge, UK, 2013.

(43) Perdew, J. P.; Burke, K.; Ernzerhof, M.: Generalized Gradient Approximation Made Simple. *Phys. Rev. Lett.* **1996**, *77*, 3865-3868.

(44) Monkhorst, H. J.; Pack, J. D.: Special points for Brillouin-zone integrations. *Phys. Rev. B* **1976**, *13*, 5188-5192.

(45) Grimme, S.: Semiempirical GGA-type density functional constructed with a long-range dispersion correction. *Journal of Computational Chemistry* **2006**, *27*, 1787-1799.

(46) Tkatchenko, A.; Scheffler, M.: Accurate Molecular Van Der Waals Interactions from Ground-State Electron Density and Free-Atom Reference Data. *Phys. Rev. Lett.* **2009**, *102*, 073005/1-073005/4.

(47) McNellis, E. R.; Meyer, J.; Reuter, K.: Azobenzene at coinage metal surfaces: Role of dispersive van der Waals interactions. *Phys. Rev. B* **2009**, *80*, 205414/1-205414/10.

(48) Refson, K.; Tulip, P. R.; Clark, S. J.: Variational density-functional perturbation theory for dielectrics and lattice dynamics. *Phys. Rev. B* **2006**, *73*, 155114.

(49) Gonze, X.; Charlier, J.-C.; Teter, M. P.: Interatomic force constants from first principles: The case of alpha-quartz. *Phys. Rev. B* **1994**, *50*, 13035-13038.

(50) Macrae, C. F.; Bruno, I. J.; Chisholm, J. A.; Edgington, P. R.; McCabe, P.; Pidcock, E.; Rodriguez-Monge, L.; Taylor, R.; van de Streek, J.; Wood, P. A.: Mercury CSD 2.0 - new features for the visualization and investigation of crystal structures. *J. Appl. Cryst.* **2008**, *41*, 466-470.

(51) Putz, H.; Brandenburg, K.: DIAMOND - Crystal and Molecular Structure Visualization. Crystal Impact GbR: Bonn, 1999.

(52) Spek, A. L.: Structure validation in chemical crystallography. *Acta Cryst* **2009**, *D65*, 148-155.

(53) Wolff, S. K.; Grimwood, D. J.; McKinnon, J. J.; Turner, M. J.; Jayatilaka, D.; Spackman, M. A.: CrystalExplorer (Version 3.1). University of Western Australia, 2012.

(54) Blatov, V. A.: Nanocluster analysis of intermetallic structures with the program package TOPOS. *Struct. Chem.* **2012**, *23*, 955-963.

(55) Campbell, B. J.; Stokes, H. T.; Tanner, D. E.; Hatch, D. M.: ISODISPLACE: An Internet Tool for Exploring Structural Distortions. *J. Appl. Cryst.* **2006**, *39*, 607-614

(56) Robles, N. L.; Parsons, S.; Mews, R.; Oberhammer, H.: $CH_3N=SF_2=NCH_3$: Structural, Conformational and Configurational Properties in the Gaseous and in the Condensed Phases. *Submitted for publication.* **2014**.

(57) Hagen, K.; Cross, V. R.; Hedberg, K.: The molecular structure of selenonyl fluoride, SeO_2F_2, and sulfuryl fluoride, SO_2F_2, as determined by gas-phase electron diffraction. *Journal of Molecular Structure* **1978**, *44*, 187-193.

(58) Hunter, C. A.; Sanders, J. K. M.: The nature of π-π interactions. *J. Am. Chem. Soc.* **1990**, *112*, 5525-5534.

(59) Cassoux, P.; Kuczkowski, R. L.; Creswell, R. A.: Microwave spectrum, structure, dipole moment, and quadrupole coupling constants of iminosulfur oxydifluoride. *Inorganic Chemistry* **1977**, *16*, 2959-2964.

(60) Oberhammer, O.; Glemser, O.; Klüver, H.: Molecular structure of N-chlorosulfur difluoride imide oxide [$ClNSOF_2$]. *Zeitschrift fuer Naturforschung, Teil A: Astrophysik, Physik und Physikalische Chemie* **1974**, *29*, 901-904.

(61) Höfs, H. U.; Mews, R.; Noltemeyer, M.; Sheldrick, G. M.; Schmidt, M.; Henkel, G.; Krebs, B.: Reactions of fluorinated nitriles with sulfur(II) chlorides; crystal structure of 2,4,6-tris(difluorosulfoximido)-1,3,5-triazene at 170 K. *Zeitschrift fuer Naturforschung, Teil B: Anorganische Chemie, Organische Chemie* **1983**, *38B*, 454-459.

Table 1. Crystal and refinement data. For all structures the formula is CH_3F_2NOS (M_r = 115.10); all experiments were carried out with Mo *K*a radiation (λ = 0.71073 Å) with a colourless cylindrical crystal of dimensions 1.00 × 1.00 × 1.00 mm^3.

Phase	I	II	II
Crystal data			
Crystal system, space group	Triclinic, *P*-1	Monoclinic, *C*2/*c*	Monoclinic, *C*2/*c*
Temperature (K)	140	140	100
a, *b*, *c* (Å)	5.220 (4) 6.383 (5) 7.041 (5)	11.660 (2) 7.2095 (14) 10.2122 (18)	11.6272 (6) 7.1454 (3) 10.1325 (5)
α, β, γ (°)	69.958 (13) 80.098 (14) 81.934 (15)	90 97.874 (13) 90	90 98.078 (3) 90
V ($Å^3$)	216.2 (3)	850.4 (3)	833.47 (7)
Z	2	8	8
μ (mm^{-1})	0.65	0.66	0.67
Data collection			
T_{min}, T_{max}	0.26, 0.52	0.22, 0.52	0.18, 0.51
No. of measured, independent and observed [$I > 2.0 \sigma(I)$] reflections	900, 751, 657	5167, 849, 738	5864, 1006, 936
R_{int}	0.110	0.057	0.035
$(\sin \theta/\lambda)_{max}$ ($Å^{-1}$)	0.620	0.628	0.678
Refinement			
$R[F^2 > 2\sigma(F^2)]$, $wR(F^2)$, S	0.044, 0.127, 1.06	0.043, 0.087, 1.07	0.030, 0.074, 1.05
No. of reflections	746	837	1005
No. of parameters	68	68	66
No. of restraints	12	12	9
$\Delta\rho_{max}$, $\Delta\rho_{min}$ (e $Å^{-3}$)	0.38, -0.42	0.32, -0.35	0.37, -0.34

Table 2: Observed and calculated internal bond distances (Å) and angles (°) in phase II. The experimental data refer to the structure determined at 100 K.

Bond distances	Expt.	PBE + Grimme	PBE + TS
S1—N1	1.4537 (14)	1.480	1.478
S1—O2	1.4029 (13)	1.423	1.422
S1—F3	1.5516 (11)	1.602	1.602
S1—F4	1.5550 (11)	1.611	1.609
N1—C1	1.474 (2)	1.484	1.481
Bond angles			
N1—S1—O2	120.65 (8)	120.70	120.65
N1—S1—F3	112.56 (7)	112.60	112.82
O2—S1—F3	107.55 (7)	107.95	107.65
N1—S1—F4	112.92 (7)	113.04	113.12
O2—S1—F4	107.02 (7)	106.68	106.65
F3—S1—F4	92.35 (6)	92.00	92.07
S1—N1—C1	123.84 (12)	124.01	125.67

Table 3. Selected bond distances (Å) and angles (°) in structures of sulfur oxide difluoride imides, $RNSOF_2$ as determined in the gas phase.

R	H[a] [59]	Cl[b] [60]	CN[b] [14]	SF_5[b] [12]	FSO_2[b] [11]
SN	1.466 (3)	1.484 (7)	1.498 (12)	1.478 (8)	1.475 (5)
SO	1.420 (5)	1.394 (3)	1.424 (5)	1.385 (4)	1.392 (5)
SF	1.549 (2)	1.548 (3)	1.543 (6)	1.541[d]	1.529 (3)
X-N	1.023 (7)	1.715 (5)	1.34[c]	1.656 (9)	1.631 (6)
NSO	119.5 (2)	117 (3)	119[c]	120.3 (14)	116.8 (22)
FSF	93.7 (1)	92.6 (8)	93.5 (13)	96.9 (18)	95.3 (21)

a. Microwave spectroscopy.
b. Gas-phase electron diffraction.
c. Parameter constrained to *ab initio* value.
d. The mean S-F distance was refined, with differences between individual S-F distances defined by *ab initio* calculations.

Table 4: Bond distances (Å) and angles (°) in sulfur oxide difluoride imides R-A (A = $NSOF_2$) as determined in the crystalline state by X-ray diffraction. Standard uncertainties are given where listed in the references cited.

	$[A]^-$ [6]	H_3C-A[a]	$AsF_5 \cdot H_3CA$[5]	$[Mn(CO)_4A]_2$[9]	$(NCA)_3$[61 d]	[OC(F)A][18]
SN	1.405 (2)	1.454 (1)	1.498 (15)	1.434 (6)	1.487 (3)	1.492 (5)
SO	1.590 (2)	1.403 (1)	1.383 (12)	1.402 (8)	1.401 (2)	1.388 (2)
SF	1.564 (1)	1.552 (1)	1.509 (12)	1.556 (7) (6)	1.523 (2)	1.518 (12)
			1.518 (12)	1.535 (7) (6)		
XN	----	1.474 (2)	1.515 (19)[b]	2.108 (8) (6)	1.396 (4)	1.378 (6)
			1.985 (16)[c]	2.116 (8)		
NSO	122.9 (2)	120.65 (8)	121.5 (9)	126.0 (10)	117.0 (2)	118.0 (8)
XNS	----	123.8 (1)	117.2 (12)[b]	128.2		121.0 (1)
			124.0 (8)[c]			
FSF	95.3 (1)	92.55 (6)	93.9 (7)	90.6 (5)	95.4 (2)	95.3 (4)

a. This work.
b. X = C
c. X = As
d. Average over four molecules in the asymmetric unit.

Table 5: Comparison of unit cell dimensions in phases I and II at 140 K.

	a/Å	*b*/Å	*c*/Å	α/°	β/°	γ/°
Phase 1	5.220	6.383	7.041	69.958	80.098	81.934
Phase 2 (reduced)	10.212	6.854	6.854	63.46	83.31	83.81
Phase 2 (standard)	11.660	7.2095	10.2122	90	97.874	90

Table 6: Intermolecular contact distances (Å) and energies (kJ mol^{-1}) in phases I and II at 140 K. Labels, A, B, C *etc.* are in order of total contact energy; the same labelling scheme is used in the Figures. The energy terms are taken from PIXEL calculations. Only interatomic contacts within 0.2 Å of the sum of the van der Waals radii of the contacting atoms (given in square brackets) are listed.

Label	Symm. Op.	E_{elec}	E_{Pol}	E_{Disp}	E_{Rep}	E_{Total}	Interatomic Contacts
Phase I (contacts formed within layers)							
A	–x, –y,1–z	–13.1	–2.6	–19.1	10.0	–24.7	S1 ... N1 3.517(4) [3.35]
C	–x,1–y, –z	–4.7	–0.8	–12.1	3.4	–14.1	S1 ... F4 3.468(4) [3.27]
D	1+x, y, z	–6.7	–1.8	–10.3	4.7	–14.1	F3 ... O2 3.112(4) [2.99] H13 ... O2 2.79(3) [2.72]
E	–1+x, y, z	–6.7	–1.8	–10.3	4.7	–14.1	O2 ...F3 3.112(4) [2.99] O2 ...H13 2.79(3) [2.72]
G	–x+1, –y, –z+1	–0.4	–1.0	–9.9	2.7	–8.6	None
H	1–x, 1–y, –z	–0.7	–0.9	–7.5	2.7	–6.4	F4 ... H12 2.79(2) [2.67]
Phase I (contacts formed between layers)							
B	–x,1–y,1–z	–10.2	–2.3	–11.4	6.8	–17.1	N1 ... H11 2.88(3) [2.75]
F	–x, –y, –z	–4.9	–1.3	–11.0	6.5	–10.6	F3 ... O2 3.163(5) [2.99] O2 ... O2 3.164(5) [3.04]
I	–x+1 –y, –z	–1.4	–0.1	–4.4	0.3	–5.6	None

Table continued on following page

Phase II (contacts formed within layers)							
A	½–x, ½–y,1–z	–15.2	–3.3	–22.1	14.4	–26.2	S1 ... N1 3.443(2) [3.35] C1 ... O2 3.410(4) [3.22]
B	½–x, –½+y, ½–z	–8.3	–2.5	–13.3	8.3	–15.8	F4 ... C1 3.364(4) [3.17] F4 ... H11 2.77(3) [2.67] H13 ... N1 2.80(2) [2.75]
C	½–x, ½+y, ½–z	–8.3	–2.5	–13.3	8.3	–15.8	N1 ... H13 2.80(2) [2.75] C1 ... F4 3.364(4) [3.17] H11 ... F4 2.77(3) [2.67]
D	½–x, ½–y, –z+1	–1.4	–0.8	–13.0	2.4	–12.8	None
H	x, –y, ½+z	0.4	–0.4	–7.1	1.8	–5.4	F3 ... N1 3.184(3) [3.02]
I	x, –y, –½+z	0.4	–0.4	–7.2	1.8	–5.4	N1 ... F3 3.184(3) [3.02]
Phase II (contacts formed between layers)							
E	–x, –y,1–z	–3.8	–1.0	–10.6	4.8	–10.6	F3 ... O2 3.095(3) [2.99]
F	–½+x, ½+y,z	–5.2	–0.8	–4.3	1.8	–8.6	O2 ... C1 3.348(4) [3.22] O2 ... H12 2.89(3) [2.72]
G	½+x, –½+y,z	–5.2	–0.8	–4.3	1.8	–8.6	C1 ... O2 3.348(4) [3.22] H12 ... O2 2.89(3) [2.72]
J	–x,y, ½–z	1.8	–0.4	–6.5	1.3	–3.8	F4 ... F4 3.034(3) [2.94]

Table 7: Comparison of optimised cell dimensions from DFT-D calculations with experimentally observed values at 140 K. Δa *etc*. represent the differences expressed as percentages, *e.g.* $\Delta a = 100(a_{\mathrm{calc}} – a_{\mathrm{obs}})/ a_{\mathrm{obs.}}$ The dimensions given for phase II refer to those of the reduced, primitive, setting.

Phase I						
	a/Å	Δa (%)	b/Å	Δb (%)	c/Å	Δc (%)
Grimme	5.156	-2.03	6.204	-2.80	6.973	-0.97
TS	5.262	0.79	6.370	-0.20	7.085	0.62
Expt	5.220		6.383		7.041	
	α/°	$\Delta\alpha$ (%)	β/°	$\Delta\beta$ (%)	γ/°	$\Delta\gamma$ (%)
Grimme	69.64	-0.45	80.03	-0.08	81.66	-0.34
TS	69.72	-0.35	80.02	-0.10	81.64	-0.36
Expt	69.96		80.10		81.93	
	V/Å^3	ΔV (%)				
Grimme	205.0922	-5.17				
TS	218.4039	0.99				
Expt	216.2697					
Phase II						
	a/Å	Δa (%)	b/Å	Δb (%)	c/Å	Δc (%)
Grimme	6.770	-1.24	6.770	-1.24	10.265	0.51
TS	6.935	1.18	6.935	0.01	10.413	1.97
Expt	6.854		6.854		10.212	
	α/°	$\Delta\alpha$ (%)	β/°	$\Delta\beta$ (%)	γ/°	$\Delta\gamma$ (%)
Grimme	97.73	1.08	97.73	1.08	61.97	-2.34
TS	97.27	0.60	97.27	0.60	62.49	-1.52
Expt	96.69		96.69		63.46	
	V/Å^3	ΔV (%)				
Grimme	410.1	-3.55				
TS	439.3	3.32				
Expt	425.2					

Figure 1: Molecular structure of $MeNSOF_2$ in phase II at 100 K. Ellipsoids enclose 50% probability surfaces.

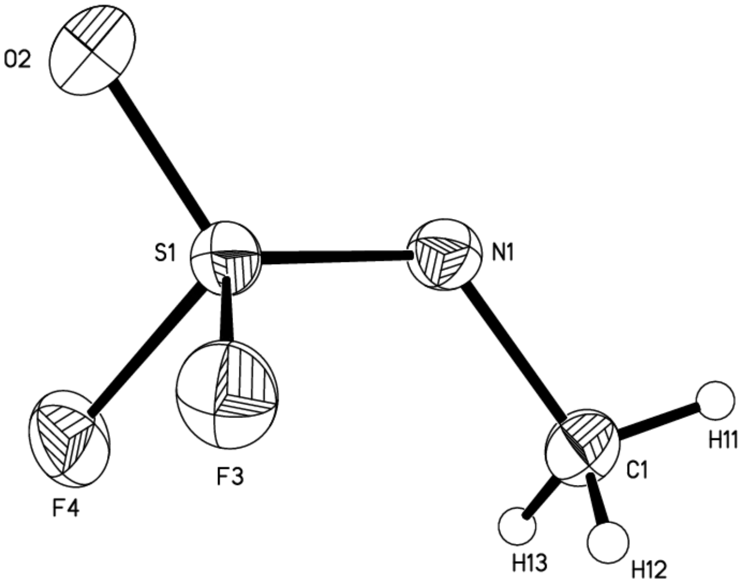

Figure 2: Structures of phases I (a) and II (b) viewed along **a** and **c**, respectively.

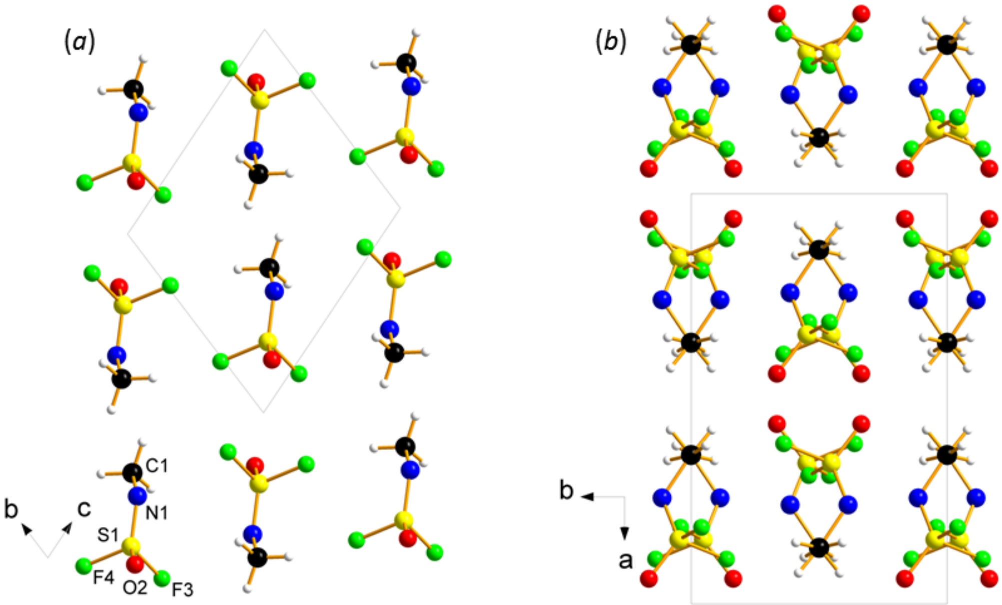

Figure 3: Layers in phases I (a) and II (b) at 140 K viewed along **b**+**c** and **a**, respectively. Corresponding plots showing Hirshfeld surfaces coloured according to the electrostatic potential. The range plotted is -0.005 au (red) to +0.005 au (blue).

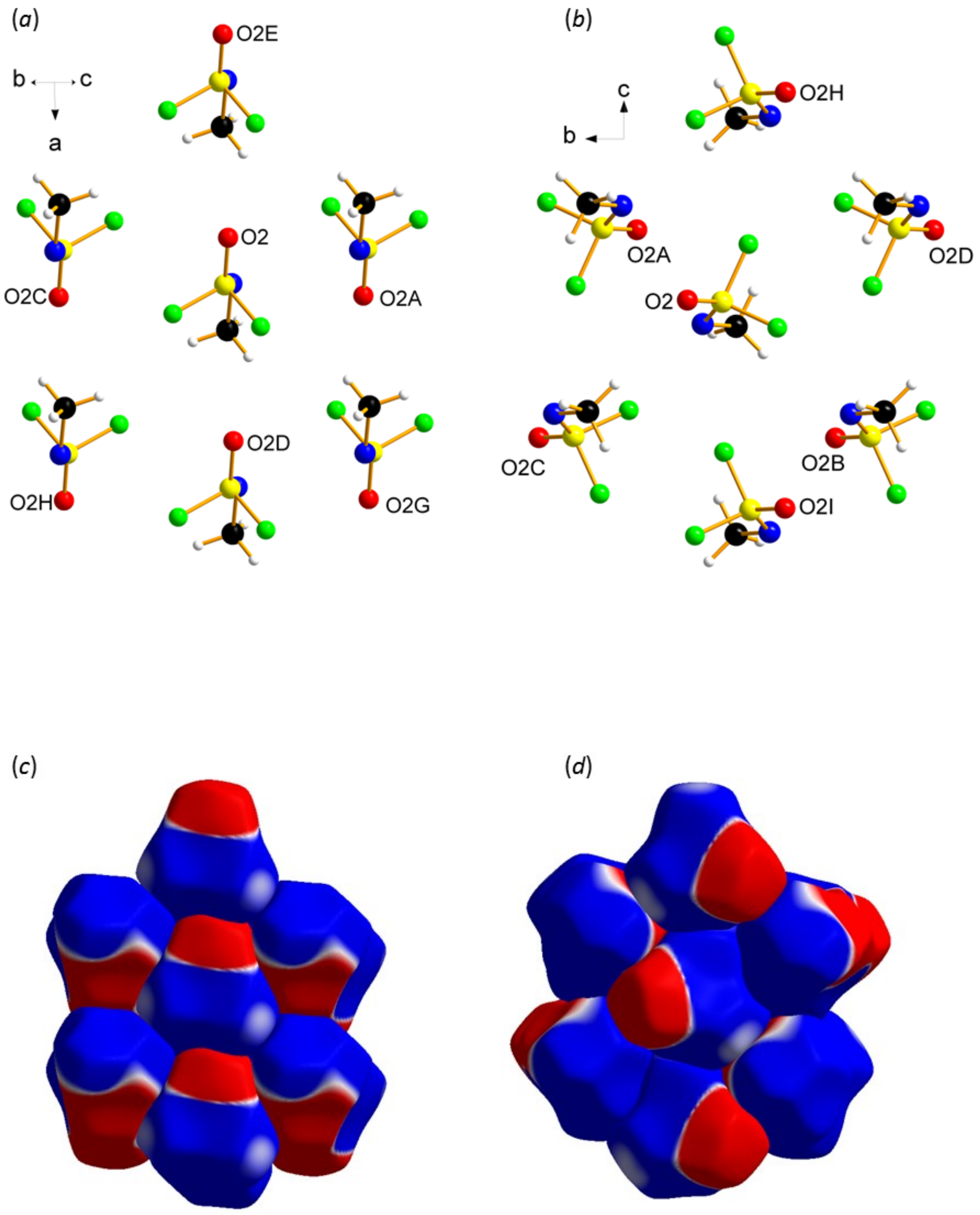

Figure 4: Principal inter-layer interactions in phases I (a) and II (b) at 140 K, together with the corresponding Hirshfeld surfaces mapped according to electrostatic potential. The colour scale used for the electrostatic potential is the same as in Fig. 3.

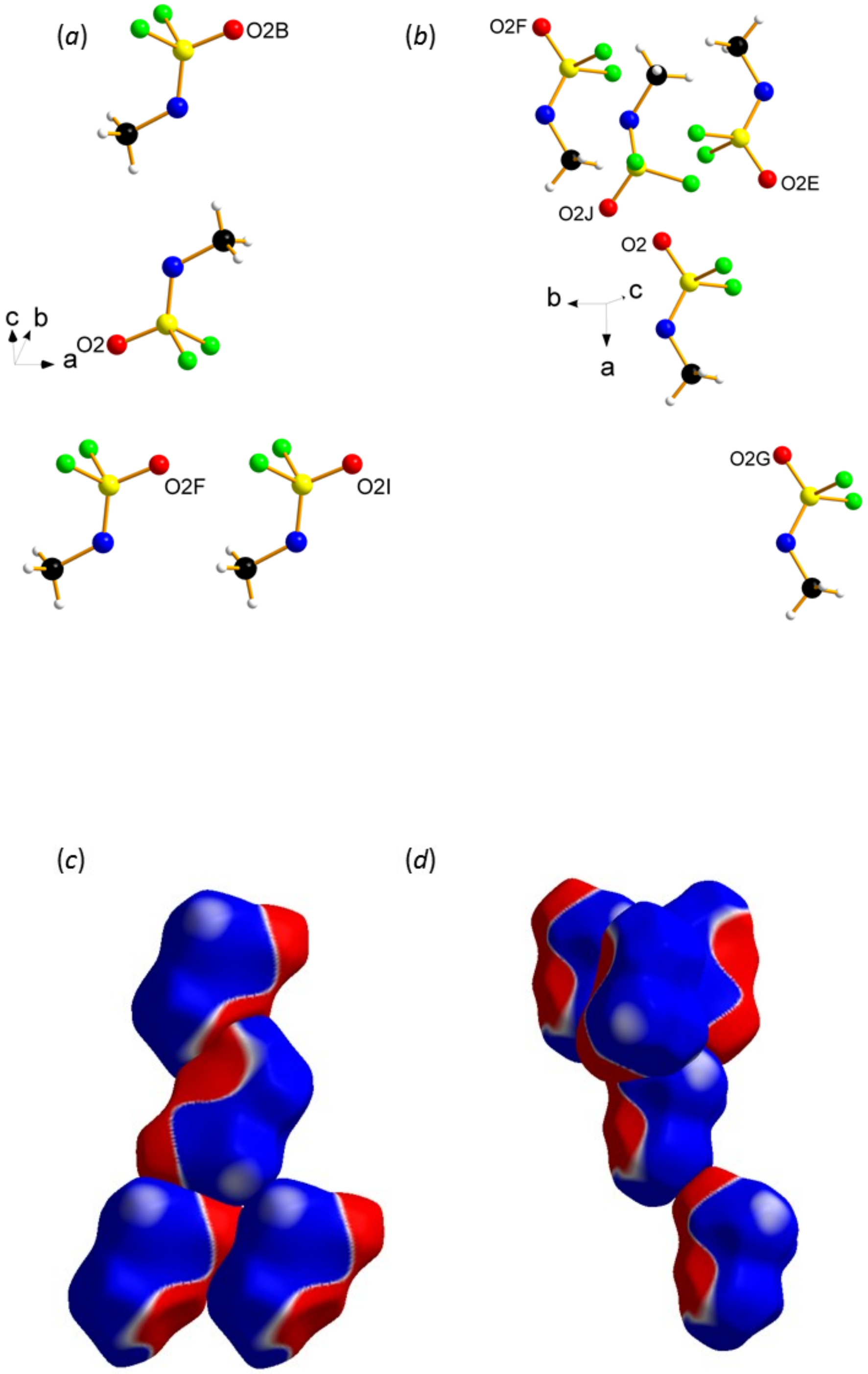

Figure 5: Variation of $\Delta G_{\mathrm{Thermal}}$ with temperature. Data calculated by DFT.

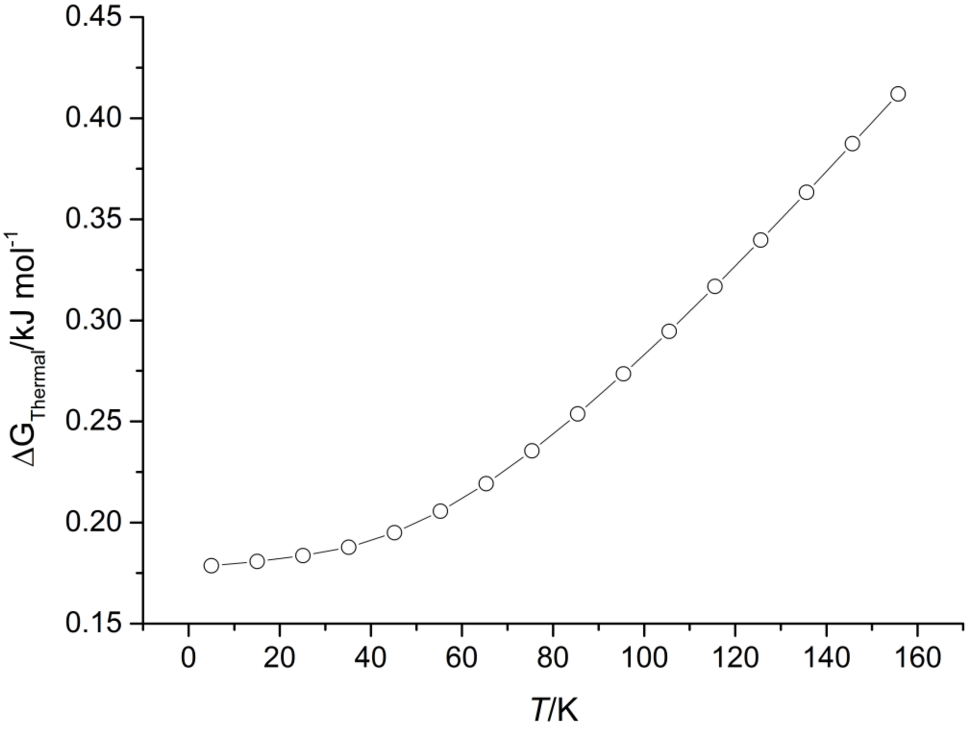

Figure 6: Partial phonon dispersion curve for phase I along the line (0 0 0) to (½ 0 0). Only vibrations with a frequency of 80 cm^{-1} and below are shown. Data calculated by DFT.